EFFECT OF FLOW-TUBE GEOMETRY ON SOLAR WIND PROPERTIES

Letter to the Editor

Y. CHEN and Y.Q. HU
Department of Earth and Space Sciences, University of Science and Technology of China, Hefei, Anhui 230026, China

(Received 5 January 2001; accepted 18 January 2002)

Abstract. A mathematical description of the solar wind flow-tube geometry is proposed. The expansion factor of the flow tube $f(r)$ ($= a/r^2$, r is the heliocentric distance and a is the flow-tube cross-section area) increases monotonically from 1 at the coronal base to f_m at r_c, and approaches its asymptotic value f_∞ nearly in a width of $2\sigma_c$. The flow tube with $f_m = f_\infty$ is demonstrated to be approximately equivalent to that given by Kopp and Holzer (1976) for the fast solar wind, and it presumably represents slow wind tubes as f_m is substantially larger than f_∞. In terms of an Alfvén wave-driven solar wind model, the effect of the flow-tube geometry on solar wind properties is examined. It is found that with the same flow conditions at the coronal base an expansion factor which increases monotonically with the radial distance results in a fast solar wind solution, whereas a flow tube which undergoes an expansion-contraction-reexpansion process creates a slow solar wind solution. Among the four flow-tube parameters the maximum expansion factor f_m has the strongest effect, and the associated Laval-nozzle formed by the contraction and reexpansion of the flow tube plays a crucial role in determining solar wind properties. It is suggested that one must take the effect of the flow-tube geometry into account while constructing reasonable flow-tube models for the slow solar wind.

1. Introduction

It is well known that the slow and fast solar winds have completely different properties. The slow wind is characterized by a high density, low flow velocity and proton temperature, large proton flux, and high variability in the flow conditions as compared to the fast wind (Bame et al., 1977; Feldman et al., 1977). It was conjectured that the slow wind would have different sources on the Sun and different acceleration and heating mechanisms in the corona (e.g. Gosling, 1996).

The cascade model of Alfvén waves proposed by Tu et al. (1984) and Tu (1987) serves as a plausible and well-considered driving mechanism for the solar wind, and was used to explain the extended heating of the solar wind plasma and the radial evolution of the Alfvén fluctuation spectrum (Tu, 1987, 1988; Hu et al., 1999), and the preferential acceleration and heating of the heavy ions near the Sun (Hu and Habbal, 1999; Hu et al., 2000) as well. However, these studies were limited to the fast solar wind. As observed by Helios spacecraft, the Alfvén waves exist in both fast and slow wind regions (Marsch et al., 1981; Roberts, 1987), but the slow

Astrophysics and Space Science **282:** 447–460, 2002.

wind is not so efficiently accelerated and heated as the fast wind is. Then, what is the main cause responsible for such discrepancy? To answer this question, Chen and Hu (2001, referred to as Paper I hereinafter) carried out a two-dimensional numerical simulation of the Alfvén wave-driven solar wind. They also presented a one-dimensional analysis for two flow tubes of distinctive geometries, and the solutions obtained with the same coronal base conditions corresponded to a fast wind and a slow one, respectively. This indicated that the flow-tube geometry plays a decisive role in generating the low proton temperature and flow velocity and high proton flux inherent to the slow solar wind. Nevertheless, the mathematical description of the flow-tube geometry proposed in paper I is limited to the slow wind case and inconvenient for a comprehensive study of the effect of the flow-tube parameters on solar wind properties.

On the basis of paper I, the present study presents a systematic analysis of the effect of the flow-tube geometry on solar wind properties. The basic equations and a new mathematical description of the flow-tube geometry are addressed in Section 2, and the numerical results are discussed in Section 3. Concluding remarks are given in Section 4.

2. Physical Model and Boundary Conditions

The one-dimensional, time dependent, MHD equations describing an electron-proton solar wind in the presence of Alfvén waves can be written in the form

$$\frac{\partial n}{\partial t} + \frac{1}{a}\frac{\partial}{\partial r}(nva) = 0, \tag{1}$$

$$\frac{\partial v}{\partial t} + v\frac{\partial v}{\partial r} + \frac{k}{nm_p}(T_e + T_p)\frac{\partial n}{\partial r} + \frac{k\partial(T_e + T_p)}{m_p \partial r} + \frac{1}{nm_p}\frac{\partial p_w}{\partial r} + \frac{GM}{r^2} = 0, \tag{2}$$

$$\frac{\partial T_e}{\partial t} + v\frac{\partial T_e}{\partial r} + \frac{\gamma - 1}{a}T_e\frac{\partial}{\partial r}(va) - \frac{\gamma - 1}{nka}\frac{\partial}{\partial r}\left(\kappa_e a\frac{\partial T_e}{\partial r}\right) + \nu_E(T_e - T_p) = 0, \tag{3}$$

$$\frac{\partial T_p}{\partial t} + v\frac{\partial T_p}{\partial r} + \frac{\gamma - 1}{a}T_p\frac{\partial (va)}{\partial r} + \nu_E(T_p - T_e) - \frac{\gamma - 1}{nk}Q = 0, \tag{4}$$

$$\frac{\partial p_w}{\partial t} + \frac{1}{a}\frac{\partial}{\partial r}[(v + v_{Ar})ap_w] + \frac{p_w}{2a}\frac{\partial}{\partial r}(va) + \frac{Q}{2} = 0. \tag{5}$$

Neutrality and zero current are assumed so that $n_e \approx n_p = n$ and $v_e \approx v_p = v$. n is the number density, v the flow velocity, T_e and T_p the electron and proton temperatures, $p_w = \rho\langle\delta v^2\rangle/2$ the Alfvén wave pressure, M, G, k, and γ are the Sun's mass, the gravitational constant, the Boltzman constant, and the adiabatic index

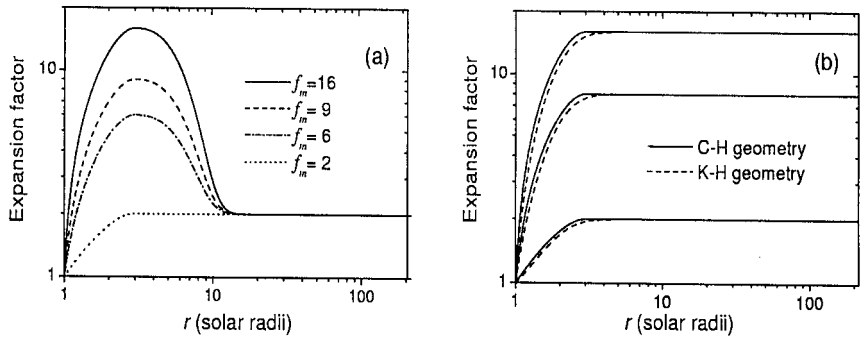

Figure 1. (a) The expansion factor of the flow tubes versus r given by Equation (6) for several separate values of f_m with $r_c = 3R_s, \sigma_c = 4.2R_s$ and $f_\infty = 2$; (b) Comparison between the expansion factor profiles expressed by Equation (6) with $f_m = f_\infty$ and $r_c = 3R_s$ in solid and by Equation (7) with $\sigma = 0.51R_s$ and $r_1 = 1.31R_s$ in dashed for $f_m = 2$, 8, and 16.

($\gamma = 5/3$) respectively, and ν_E the electron-proton collision frequency taken to be $9.094 \times 10^{-8} n T_e^{-3/2}$ (Braginskii, 1965), where n is in the unit of m^{-3} and T_e, in the unit of K. Following Hu et al. (1997), we use the classical thermal conductivity for electrons (Spitzer, 1962) and ignore the proton thermal conduction.

The flow tube cross-section area is given by $a = r^2 f(r)$, where $f(r)$ is the expansion factor. In this study, we construct the following expansion factor:

$$f(r) = \begin{cases} f_m - (f_m - 1)(r - r_c)^2/(r_c - R_s)^2, & r < r_c, \\ f_\infty + (f_m - f_\infty)\exp[-(r - r_c)^2/\sigma_c^2], & r \geq r_c, \end{cases} \tag{6}$$

where f_m, f_∞, r_c, and σ_c are the parameters of the flow tube. Such an expansion factor increases monotonically from 1 at the coronal base to f_m at r_c, and then approaches an asymptotic value f_∞ in a width of $2\sigma_c$. For slow wind tubes, r_c is close to the radial distance of the Y-type neutral point of the helmet streamer. With $r_c = 3R_s$, $\sigma_c = 4.2R_s$, and $f_\infty = 2$, the radial profiles of the expansion factor are shown in Figure 1a for several separate values of f_m. When $f_m = 2$ ($= f_\infty$), $f(r)$ remains constant after it reaches f_m at r_c, as shown in Figure 1a by the dotted curve. The expansion factor defined by Kopp and Holzer (1976), i.e.

$$f_1(r) = \frac{f_m e^{(r-r_1)/\sigma} + 1 - (f_m - 1)e^{(R_s - r_1)/\sigma}}{e^{(r-r_1)/\sigma} + 1} \tag{7}$$

was extensively used in literature for the study of the fast solar wind. Hereinafter, the two flow tubes defined by Equations (6) and (7) are called C-H tube and K-H tube for short, respectively. To some extent, the K-H tube may be approximately considered as a special case of the C-H tube by taking $f_m = f_\infty$ and a suitably selected r_c based on the values of r_1 and σ for the K-H tube. Incidentally, the value of σ_c does not affect $f(r)$ in this case. For instance, given $r_1 = 1.31R_s$ and

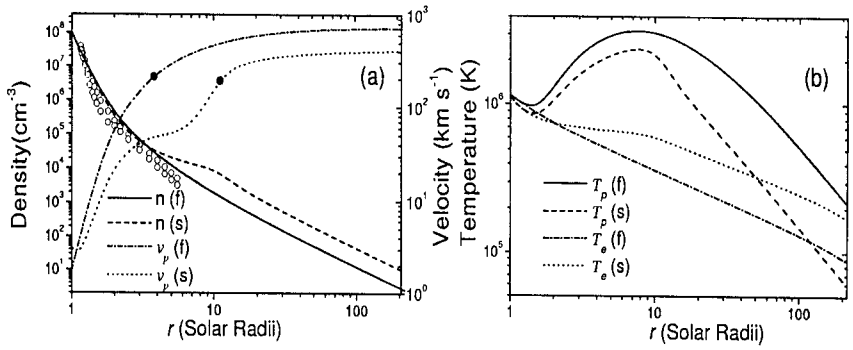

Figure 2. Radial profiles of (a) the density and velocity, (b) the proton and electron temperatures. The expansion factors for tubes f and s are shown in Figure 1 with $f_m = 2$ and 16 respectively. The solid circles in Figure 2a denote the critical point of sound speed. The open circles correspond to the upper and lower limits of density inferred from white light coronagraph observations (Fisher and Guhathakurta, 1994).

$\sigma = 0.51R_s$, we may take $r_c = 3R_s$. The resultant profiles of $f(r)$ and $f_1(r)$ are shown in Figure 1b by solid and dashed curves, respectively, for $f_m = 2$, 8 and 16. The two sets of expansion factors turn out to be very close to each other. A small discrepancy does exist in the near Sun region below $r_c = 3R_s$, but it has no appreciable influence on the obtained solutions, as will be demonstrated in Section 3.1.

Following the practice of Paper I, we adopt the Kolmogorov rate (Hollweg, 1986) as the dissipation rate of the Alfvén waves, expressed by

$$Q = \rho \langle \delta v^2 \rangle^{3/2} / L_c \tag{8}$$

where $\langle \delta v^2 \rangle$ is the velocity variance associated with the wave field, and L_c is the correlation length of the fluctuations given by $L_c = L_{c0}(B_c/B)^{1/2}$ (B_c is the magnetic field strength at the coronal base and L_{c0} is set to be 1.05×10^5 km in this study).

In order to achieve a better resolution near the Sun, a non-uniform mesh with $N = 500$ grid points is laid out from $1R_s$ to 1.2 AU. The grid spacing increases monotonically from $4.5 \times 10^{-4}R_s$ at the base to $1.96R_s$ at $100R_s$ in terms of a geometric series of common ratio 1.02, and then remains invariant up to 1.2 AU. The boundary conditions at the coronal base are specified as follows: $n_0 = 1 \times 10^8$ cm^{-3}, $T_0 = 1.14 \times 10^6$ K, $B_0 = 1.6 f_\infty$ G, and $p_{w0} = 7.5 \times 10^{-4}$ dyn cm^{-2} that is equivalent to a wave amplitude $\langle \delta v^2 \rangle^{1/2} = 30$ km s^{-1}. Equations (1)–(5) are solved by the time-dependent method developed by Hu et al. (1997).

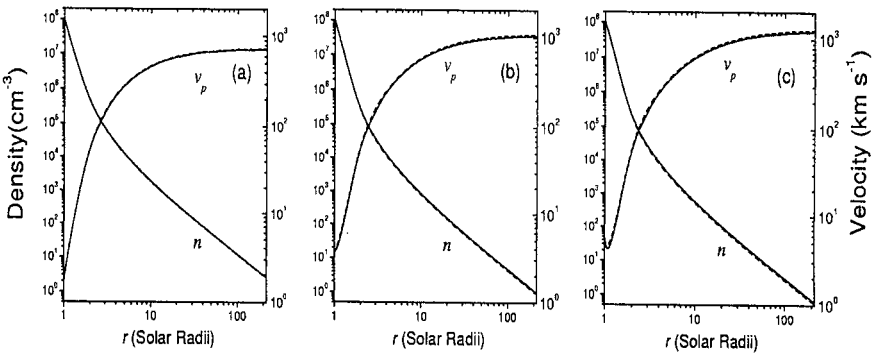

Figure 3. Comparison between density and velocity profiles of the solutions for the three pairs of tubes shown in Figure 1b: (a) $f_m = 2$, (b) $f_m = 8$, $f_m = 16$.

3. Numerical Results

In order to study the effect of the flow-tube geometry on solar wind properties, we keep the coronal base conditions the same for all numerical examples to be mentioned below. Two C-H tubes are singled out from those depicted in Figure 1a with $f_m = 2$ and 16, called tube f and tube s respectively. The steady solar wind solutions obtained for the two flow tubes are depicted in Figures 2a and 2b respectively. The density and velocity profiles are shown in Figure 2a by solid and dot-dashed curves for tube f and by dashed and dotted curves for tube s, respectively, whereas the proton and electron temperature profiles are shown in Figure 2b by solid and dot-dashed curves for tube f and by dashed and dotted curves for tube s, respectively. The solution associated with tube f yields the following parameters at 1 AU: $nv = 1.88 \times 10^8$ cm^{-2} s^{-1}, $n = 2.63$ cm^{-3}, $v = 717$ km s^{-1}, $T_e = 8.70 \times 10^4$ K, $T_p = 2.17 \times 10^5$ K, and $\langle \delta B^2 \rangle / B^2 = 0.76$, and the solution associated with tube s yields $nv = 3.82 \times 10^8$ cm^{-2} s^{-1}, $n = 9.40$ cm^{-3}, $v = 406$ km s^{-1}, $T_e = 1.71 \times 10^5$ K, $T_p = 5.95 \times 10^4$ K, and $\langle \delta B^2 \rangle / B^2 = 0.66$. The predicted parameters essentially agree with the observations for the fast and slow winds respectively (Schwenn, 1991; Villante and Vellante, 1982). The open circles in Figure 2a denote the data of electron density in the fast wind inferred by Fisher and Guhathakurta (1994). The predicted number density profile is higher than observed, implying an insufficient acceleration by the Alfvén waves in the inner corona, a common deficiency inherent in other wave-driven solar wind models (Esser et al., 1987; Hu et al., 1999). The two density profiles are almost the same below $3R_s$ but diverge beyond. The former stems from the fact that a larger mass flux and a lower flow velocity in tube s compensate for the fall of the density profile in the region below $3R_s$ caused by the rapid expansion of the tube. On the other hand, the rapid contraction of tube s beyond $3R_s$ substantially slows down the decay of the density profile there. As seen from Figure 2b, T_p is higher than

T_e in the fast wind and T_p is lower than T_e beyond 50 R_s in the slow wind, which agrees well with the Ulysess/SWOOPS measurements (Phillips et al., 1995). The solid circles in the velocity profiles of Figure 2a denote the critical point of sound speed, 3.83 R_s with the critical sound speed 209 km s^{-1} for the fast wind and 11.2 R_s with the critical sound speed 189 km s^{-1} for the slow wind. As mentioned previously, the C-H tube includes the K-H tube approximately as a special case. To further confirm this conclusion, we take the three pairs of flow tubes given in Figure 1b and show the density and flow velocity profiles for the corresponding steady solar wind solutions respectively. Again, the solutions associated with the C-H tubes are depicted by solid curves and those associated with the K-H tubes by dashed curves in Figure 3. It can be seen that the solutions for the K-H tubes nearly coincide with those for the C-H tubes. Similar conclusions hold for the electron and proton temperatures, but we omit showing them to save space. In summary, we argue that a K-H tube can be always approximated by a C-H tube with $f_m = f_\infty$ and a suitably selected r_c. Therefore, one may use the C-H tube to achieve a unified investigation of the effect of the tube geometries on the solar wind properties, as we did in this study.

3.1. Effect of the flow-tube geometry on solar wind properties

To explore the effect of the flow-tube geometry on solar wind properties, we use the C-H geometry, and adjust one of the four parameters appearing in Equation (6) in an appropriate range while keeping the others fixed at certain reference values, which are chosen to be $f_m = 16$, $r_c = 3R_s$, $\sigma_c = 4.2R_s$, and $f_\infty = 2$, respectively. A flow tube associated with these reference values is exactly tube s as defined above.

Figure 4 shows the radial profiles of the cross-section area a of the C-H tube for various flow-tube parameters. From bottom to top, the profiles of the cross-section area a correspond to $f_m = 2$, 6, 9, 16 and 20 in Figure 4a, $r_c = 2.5$, 3.0, 3.5, 4.0 and 4.5 (R_s) in Figure 4b, $\sigma_c = 2.6$, 3.8, 5, 6.2 and 7.4 (R_s) in Figure 4c, and $f_\infty = 1.5$, 2.0, 2.5, 3.0 and 3.5 in Figure 4d, while the other unassigned parameters take their reference values. It can be seen from Figure 4 that for those profiles with a dip, the flow tube undergoes a contraction and then expands again along the radial direction, shaped like Laval-nozzle. The radial distance of the throat of the Laval nozzle increases slightly with increasing f_m (Figure 4a) and r_c (Figure 4b), but sharply with increasing σ_c (Figure 4c), whereas it decreases slightly with increasing f_∞ (Figure 4d). The existence of a Laval-nozzle somewhere in the flow tube has significant influence on solar wind properties, as will be discussed in detail below.

It is the energy flux of the Alfvén waves emitted from the solar surface that determines the energy budget, i.e. the acceleration and heating of the solar wind

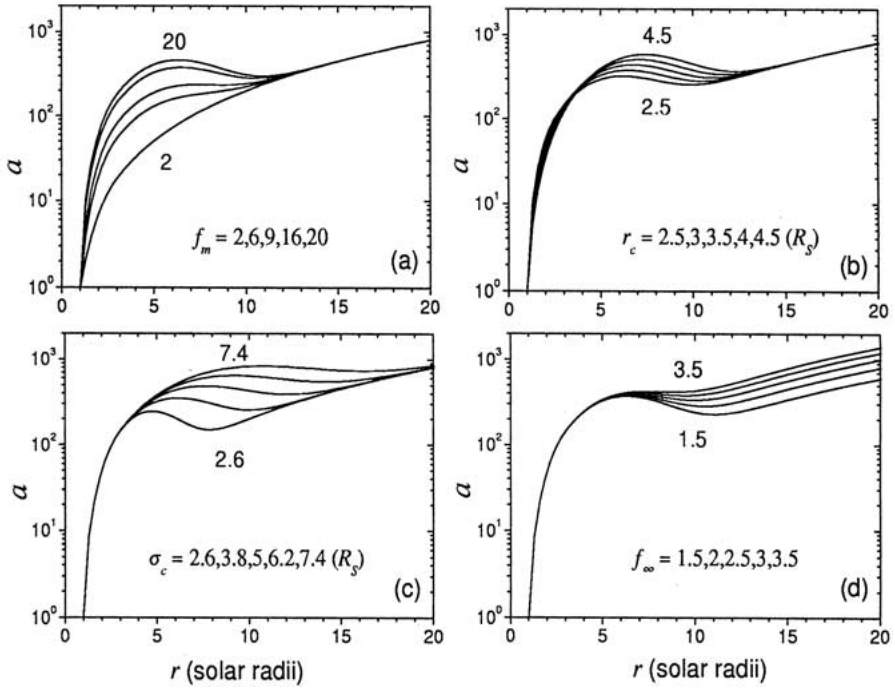

Figure 4. The radial profiles of the cross-section area of the C-H tubes for 5 separate values of (a) f_m, (b) r_c, (c) σ_c, and (d) f_∞ while the unassigned parameters take their reference values: 16, 3 R_s, 4.2 R_s, and 2 for f_m, r_c, σ_c, and f_∞, respectively.

plasma. After normalization to 1 AU, the energy flux of the Alfvén waves is given by:

$$F(r) = \frac{avp_w}{a_E}\left(3 + \frac{2}{M_A}\right), \tag{9}$$

where a_E is the cross-section area of the flow tube near the Earth, and $M_A = v/v_A$, v_A is the Alfvén wave speed. $F(R_s) \approx 2a_0 v_{A0} p_{w0}/a_E$ represents the energy flux of the Alfvén waves emitted from the coronal base, which is almost exhausted within 1 AU, namely, F (1 AU) ≈ 0. Define

$$g(r) = \frac{F(R_s) - F(r)}{F(R_s)}, \tag{10}$$

that represents the proportion of the wave energy flux deposited in the region between 1 R_s and r. Obviously, we have $g(R_s) = 0$ and $g(r = 1\text{ AU}) \approx 1$.

3.1.1. *Effect of the maximum expansion factor*

Adjusting f_m from 2 to 22, and fixing the other parameters at their reference values, we obtain a group of solar wind solutions. The parameters at 1 AU as a

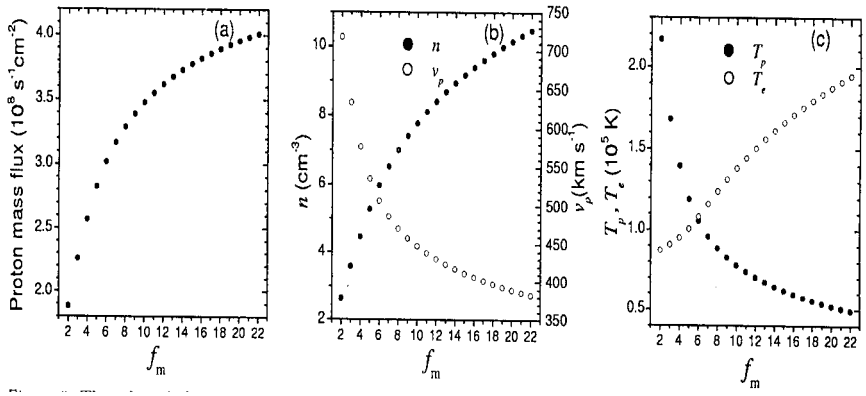

Figure 5. The solar wind properties at 1 AU versus the maximum expansion factor f_m with $r_c = 3R_s$, $\sigma_c = 4.2R_s$ and $f_\infty = 2$.

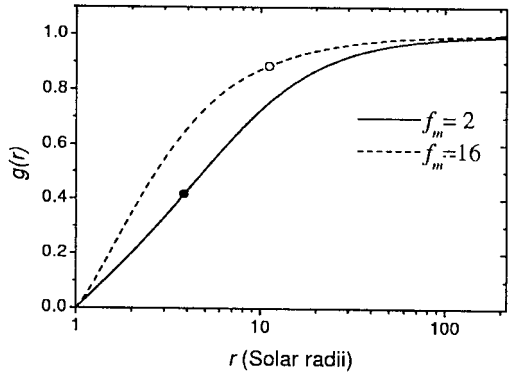

Figure 6. Radial profiles of $g(r)$ for the flow tubes of $f_m = 2$ and 16 with $r_c = 3R_s$, $\sigma_c = 4.2R_s$ and $f_\infty = 2$. The solid and open circles denote the critical points associated with $f_m = 2$ and 16 respectively.

function of f_m are shown in Figure 5. The proton flux, number density and electron temperature increase and the flow velocity and proton temperature decrease with increasing f_m, in other words, the solution tends to the slow wind as f_m increases. Figure 6 shows $g(r)$ (see Equation (10)) for tube f ($f_m = 2$) and s ($f_m = 16$). The solid and open circles in Figure 6 denote the critical points associated with $f_m = 2$ and 16 respectively. The radial distance of the critical point versus f_m is shown in Figure 7 by solid circles. It can be seen from Figures 6 and 7 that as f_m increases, the critical point moves outward away from the Sun, the deposition region of the wave energy moves towards the Sun, and thus the solar wind tends to the slow wind. As pointed out by Leer and Holzer (1980), an input of momentum and energy in the supersonic flow region leads to an increase of the solar wind

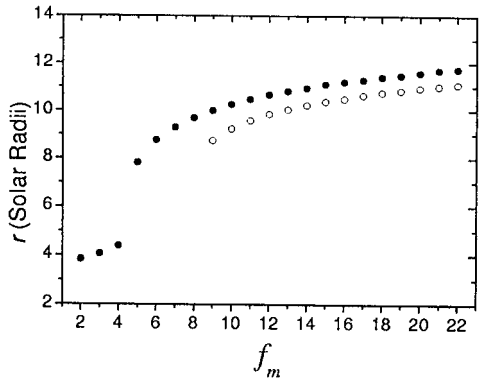

Figure 7. The radial distances of the critical point (solid circles) and the throat of the Laval nozzle (open circles) versus f_m while taking the other parameters to be their reference values ($r_c = 3R_s$, $\sigma_c = 4.2R_s$, and $f_\infty = 2$).

velocity and a decrease of the proton flux at 1 AU. On the contrary, the wind velocity will decrease and the proton flux will increase at 1 AU if momentum and energy are added in the subsonic flow region. This conclusion is consistent with the numerical results described above. Taking $v_p > 500$ km s^{-1} as a criterion for the fast wind, the solutions associated with $f_m < 6$ in Figure 5 is then approximately taken for the fast wind, and those associated with $f_m > 6$ for the slow wind. As seen from Figure 4a, the flow tube is shaped like a Laval nozzle for $f_m \geq 9$. The radial distance of the throat of the Laval nozzle versus f_m is shown in Figure 7 by open circles. The critical point lies outside the throat for $f_m \geq 9$, implying that the Laval nozzle formed by the contraction and reexpansion of the flow tube does play an important role in determining solar wind properties. The reason is as follows: outside the throat of the Laval nozzle (about $10R_s$), the influence of the gravity and Alfvén waves on the solar wind are substantially weakened so that the Laval-nozzle effect becomes dominant. Incidentally, even if the Laval nozzle does not appear for $f_m < 9$, the critical point still moves outward while f_m increases, as clearly seen from Figure 7. This is due to a less than spherical expansion of the flow tube for a larger value of f_m, which causes the outward shift of the critical point.

3.1.2. *Effect of the location of the maximum expansion factor*

The height of the helmet streamer is estimated to be about 3 R_s by Koutchmy and Livshits (1992), so we have taken a reference value of 3 R_s for r_c. Through adjusting r_c from 2.5 to 4.5 R_s and keeping the other three parameters fixed at their reference values, another group of solutions are obtained. Figure 8 shows the dependence of the solar wind parameters at 1 AU on r_c. All solution are close to the slow wind, implying that the effect of r_c on solar wind properties at 1 AU is small. The radial distances of the critical point of sound speed and the throat of the Laval nozzle are shown in Figure 9. The critical point of sound speed is always

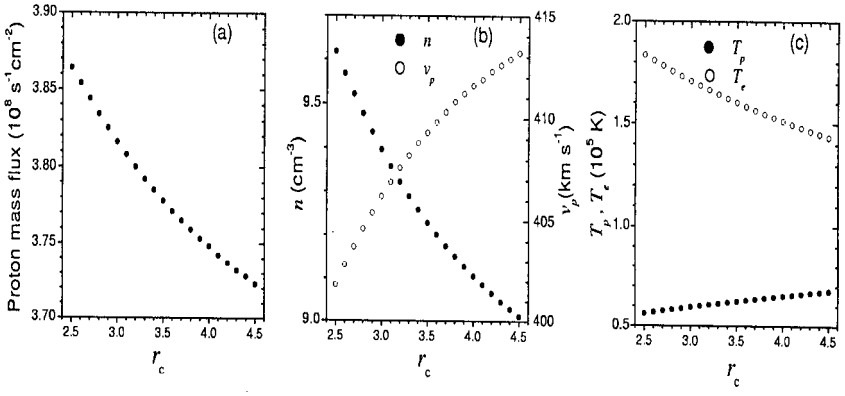

Figure 8. The solar wind properties at 1 AU versus r_c with $f_m = 16$, $\sigma_c = 4.2R_s$ and $f_\infty = 2$.

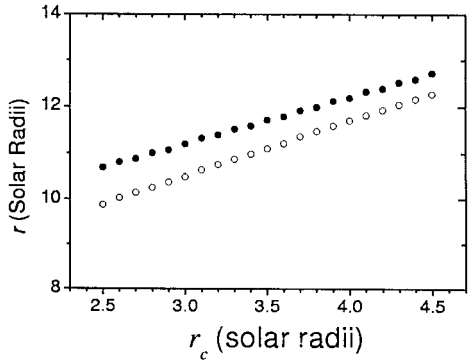

Figure 9. The radial distances of the critical point (solid circles) and the throat of the Laval nozzle (open circles) versus r_c while taking the other parameters to be their reference values ($f_m = 16$, $\sigma_c = 4.2R_s$, and $f_\infty = 2$).

located inside the corresponding throat of the Laval nozzle, implying a dominant role taken by the Laval nozzle as mentioned above. The profiles of $g(r)$ for $r_c = 2.5$ and 4.5 R_s are shown in Figure 10, and the corresponding critical points are marked by a solid and an open circle, respectively. As seen from Figure 10, the increase of r_c has two effects: (1) The critical point of sound speed moves outward, and (2) The spatial distribution of the wave energy deposition changes. The first effect leads to a slight increase of the wave energy deposition in the subsonic flow region: $g(r)$ at the critical point increases from 0.879 for $r_c = 2.5R_s$ to 0.894 for $r_c = 4.5R_s$. On the other hand, the increase of r_c results in a shift of the wave energy deposition away from the Sun within the subsonic flow region. The second effect dominates so that more energy is deposited at larger distances. As a result, the number density decreases, and the flow velocity and the proton temperature

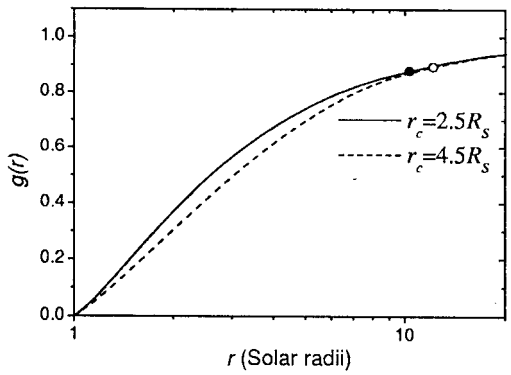

Figure 10. Radial profiles of $g(r)$ for the two flow tubes of $r_C = 2.5$ and 4.5 R_S with $f_m = 16$, $\sigma_C = 4.2R_S$ and $f_\infty = 2$. The solid and open circles denote the critical points associated with $r_C = 2.5$ and 4.5 R_S respectively.

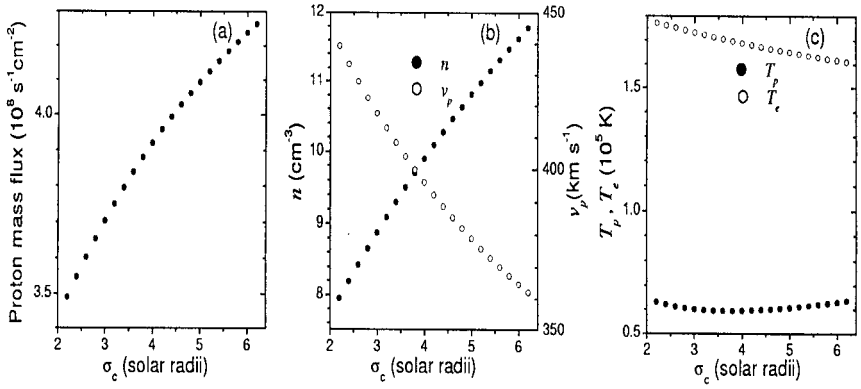

Figure 11. The solar wind properties at 1 AU versus σ_C with $f_m = 16$, $r_C = 3R_S$ and $f_\infty = 2$.

increase with increasing r_C, as clearly seen from Figure 8. Although the effect is small, it does tell us that the solar wind properties are determined by not only the relative amount of the wave energy deposited inside the critical point of sound speed, but the detailed spatial distribution of the stored wave energy within the subsonic flow region: the more energy is deposited in regions closer to the Sun, the more like the slow wind the obtained solution will be.

3.1.3. *Effect of the half-width of the contraction region of the flow tube*

The third group of solutions are obtained by adjusting σ_C from 2.6 to 7.4 R_S while keeping the other three parameters fixed at their reference values. The parameters at 1 AU versus σ_C are shown in Figure 11. It is found that a smaller σ_C produces a solution with a higher proton flux and number density and a lower flow velocity and electron temperature, but the effect of σ_C on solar wind properties at 1 AU

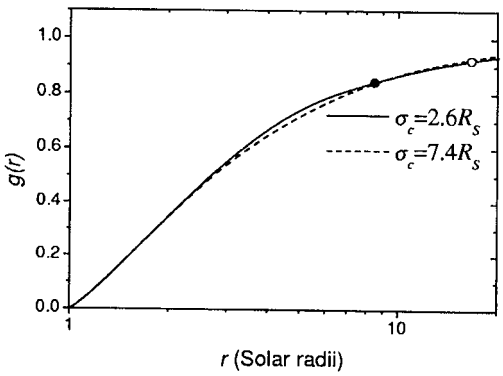

Figure 12. Radial profiles of $g(r)$ for the two flow tubes of $\sigma_c = 2.6$ and 7.4 with $f_m = 16$, $r_c = 3R_s$ and $f_\infty = 2$. The solid and open circles denote the critical points associated with $\sigma_c = 2.6$ and 7.4 R_s respectively.

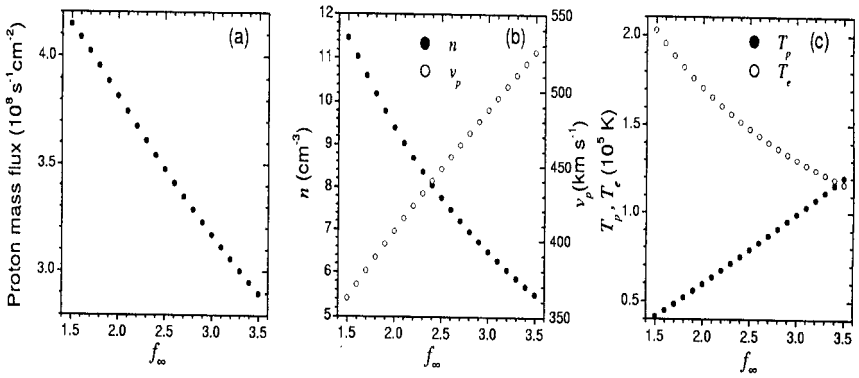

Figure 13. The solar wind properties at 1 AU versus f_∞ with $f_m = 16$, $r_c = 3R_s$ and $\sigma_c = 4.2R_s$.

turns out to be small, too. The profiles of $g(r)$ for $\sigma_c = 2.6$ and 7.4 R_s are shown in Figure 12, and the corresponding critical points are marked by a solid and an open circle, respectively. It can be seen from Figure 12 that the magnitude of σ_c has a negligible effect on the radial distribution of the deposited wave energy. In this situation, the solar wind properties rely mainly on the location of the critical point of sound speed. As shown in Figure 4c, the throat of the Laval nozzle moves outward with increasing σ_c, so does the critical point. As a result, more wave energy is deposited in the subsonic flow region for a larger value of σ_c. That's why the solution tends to the slow wind while σ_c increases.

3.1.4. *Effect of the asymptotic expansion factor*

Figure 13 shows the solar wind parameters at 1 AU as a function of f_∞ in the range of (1.5, 3.5). A larger f_∞ leads to a lower proton flux, number density and electron temperature, and a higher flow velocity and proton temperature, namely, the solution tends to the fast wind with increasing f_∞. The reason is twofold. First, to match the predicted magnetic field strength at 1 AU with observations, the magnetic field strength at the coronal base has been set to be $B_0 = 1.6 f_\infty$ G. Thus B_0 increases with increasing f_∞, resulting in an increase of the wave energy flux at the coronal base that is proportional to B_0. Secondly, from Figure 4d, the throat of the Laval nozzle moves inward with increasing f_∞, so does the critical point, and thereby the proportion of the wave energy stored in the supersonic flow region increases. Obviously, both effects are in favor of the trend of the solution towards the fast wind.

The preceding analysis was carried out for a special set of reference values of the flow-tube parameters. Similar calculations were made for other combinations of the reference parameters, and the conclusions were found to be similar to those reached above.

4. Concluding Remarks

Taking a one-dimensional flow-tube model with Alfvén waves as the common driving mechanism, we have presented a systematic analysis of the effect of the flow-tube geometry on solar wind properties. A mathematical description of the flow tube is proposed (see Equation (6)), and it involves four parameters: f_m, the maximum expansion factor, r_c, the radial distance at which f_m is located, f_∞, the asymptotic expansion factor, and σ_c, the half of the width across which the expansion factor nearly approaches f_∞. Such a flow-tube geometry approximately includes that proposed by Kopp and Holzer (1976) as a special case of $f_m = f_\infty$. The study of the effect of the flow-tube geometry on solar wind properties shows: (1) The maximum expansion factor f_m has the strongest effect on solar wind properties, and the larger f_m is, the closer the solution will be to the slow wind; (2) The Laval-nozzle effect induced by the expansion-contraction-reexpansion of the flow tube has significant effect on solar wind properties.

Our study is based on a one-dimensional Alfvén wave-driven solar wind model, in which the flow-tube geometry affects the WKB damping and the cascade dissipation of the Alfvén waves. To see whether the obtained conclusions are applicable to other heating and acceleration mechanisms, similar calculations were made based on artificially prescribed heating and acceleration functions. It was found that the flow-tube geometry can also produce similar effects on solar wind properties. Thus we argue that the conclusions reached in this study hold for other heating and acceleration mechanisms. In any case, an intimate attention must be paid to the effect of the flow-tube geometry while constructing a solar wind model.

In general, the magnetic field strength increases rapidly with latitude in the neighborhood of the Y-type neutral point, and becomes comparable with that in the polar region somewhere not too far from the equatorial plane. Correspondingly, the maximum expansion factor of the flow tubes decreases sharply with latitude. Consequently, the latitudinal width of the slow wind region and the transition layer between the slow and fast winds must be very narrow, as observed by Ulysess (Phillips et al., 1995).

Acknowledgements

The work was supported by the National Natural Science Foundation of China under grant 49974035 and the Innovation Engineering Fund of the USTC.

References

Bame, S.J., Asbridge, J.R., Feldman, W.C. and Gosling, J.T.: 1977, *J. Geophys. Res.* **8**, 1487.
Braginskii, S.I.: 1965, Transport processes in a plasma, in: M.A. Leontovich (ed.), *Reviews of Plasma Physics* **1**, Consultants Bureau, New York, p. 205.
Chen, Y. and Hu, Y.Q.: 2001, *Sol. Phys.* **199** (2), 371 (Paper I).
Esser, R., Holzer, T.E. and Leer, E.: 1987, *J. Geophys. Res.* **92**, 13377.
Feldman, W.C., Asbridge, J.R., Bame, S.J. and Gosling, J.T.: 1977, in: O.R. White (ed.), *The solar output and its variation*, Colorado Assoc. Univ. Press, Boulder, p. 351.
Fisher, R.R. and Guhathakurta, M.: 1994, *Space Sci. Rev.* **70**, 267.
Gosling, J.T.: 1996, *Robotic exploration close to the Sun: scientific basis*, p. 23.
Hollweg, J.V.: 1986, *J. Geophys. Res.* **91**, 4111.
Hu, Y.Q., Esser, R. and Habbal, S.R.: 2000, *J. Geophys. Res.* **105**, 5093.
Hu, Y.Q. and Habbal, S.R.: 1999, *J. Geophys. Res.* **104**, 17045.
Hu, Y.Q., Habbal, S.R. and Li, X.: 1999, *J. Geophys. Res.* **104**, 24819.
Hu, Y.Q., Esser, R. and Habbal, S.R.: 1997, *J. Geophys. Res.* **102**, 14661.
Kopp, R.A. and Holzer, T.E.: 1976, *Sol. Phys.* **49**, 43.
Koutchmy, S. and Livshits, M.: 1992, *Space Sci. Rev.* **61**, 393.
Leer, E. and Holzer, T.E.: 1980, *J. Geophys. Res.* **85**, 4681.
Marsch, E., Muhlhauser, K.-H., Rosenbauer, H., Schwenn, R. and Denskat, K.U.: 1981, *J. Geophys. Res.* **86**, 9199.
Phillips, J.L., et al.: 1995, *Geophys. Res. Lett.* **22**, 3301.
Roberts, D.A., Goldstein, M.L., Klein, L.W. and Matthaeus, W.H.: 1987, *J. Geophys. Res.* **92**, 12023.
Schwenn, R.: 1991, in: R. Schwenn and E. Marsch (eds.), *Physics of the Inner Heliosphere 1 Large-Scale Phenomena*, Springer-Verlag, New York, p. 99.
Spitzer, L., Jr.: 1962, *Physics of Fully Ionized Gases*, Wiley-Interscience, New York.
Tu, C.-Y. and Marsch, E.: 1987, *Space Sci. Rev.* **73**, 1.
Tu, C.-Y.: 1987, *Sol. Phys.* **109**, 149.
Tu, C.-Y.: 1988, *J. Geophys. Res.* **93**, 7.
Tu, C.-Y., Pu, Z.Y. and Wei, F.S.: 1984, *J. Geophys. Res.* **89**, 2521.
Usmanov, A.V., Goldstein, M.L., Besser, B.P. and Fritzer, J.M.: 2000, *J. Geophys. Res.* **105**, 12675.
Villante, U. and Vellante, M.: 1982, *Sol. Phys.* **81**, 367.